separations

MDPI

Article

Deep Purification of Manganese Sulfate Electrolyte by Sodium Dimethyldithiocarbamate Chelation Precipitation: Process and Selective Coordination Mechanism

Tong Liu [1,2,3], Fei Zhu [1,2,3,*], Xijun Tian [1,2,3], Zhenping Cai [1,2,3], Kai Huang [4] and Song Chen [1,2,3,*]

[1] National Engineering Research Center for Environment-Friendly Metallurgy in Producing Premium Non-Ferrous Metals, GRINM Group Corporation Limited, Beijing 100088, China; liutong1830@163.com (T.L.); tianxijun1997@163.com (X.T.); caizhenping@grinm.com (Z.C.)
[2] GRINM Resources and Environment Tech. Co., Ltd., Beijing 100088, China
[3] General Research Institute for Nonferrous Metals, Beijing 100088, China
[4] School of Metallurgical and Ecological Engineering, University of Science and Technology Beijing, Beijing 100083, China; khuang@metall.ustb.edu.cn
* Correspondence: zhufei@grinm.com (F.Z.); songch@grinm.com (S.C.)

Abstract

This study addresses the issue of insufficient product purity caused by the co-deposition of three major impurity ions—zinc, nickel, and lead—during the electrodeposition process of high-purity manganese. A targeted deep purification method for manganese sulfate electrolyte was developed using dithiocarbamate chelating agents (sodium dimethyldithiocarbamate, SDD). By optimizing key process parameters such as precipitant concentration, reaction temperature, reaction time, and solution pH, combined with density functional theory (DFT) calculations, to elucidate the selective impurity removal mechanism at the molecular level, a novel process for the efficient synergistic removal of Zn^{2+}, Ni^{2+}, and Pb^{2+} was established. The results showed that under the conditions of precipitant concentration of 1 g/L, solution pH of 6.5, reaction temperature of 55 °C, and reaction time of 2 h, the residual concentrations of Zn, Ni, and Pb in the electrolyte were all below 0.2 mg/L. DFT calculations revealed that SDD coordinates with metal ions through four sulfur atoms, and the absolute values of binding energies follow the order $Ni^{2+} > Pb^{2+} > Zn^{2+} > Mn^{2+}$, indicating thermodynamically preferential capture of impurity ions. After purification, the manganese metal obtained by electrodeposition from the manganese sulfate solution achieved a purity exceeding 99.999%, with Zn, Ni, and Pb contents of 0.11 mg/kg, 0.038 mg/kg, and 0.05 mg/kg, respectively, meeting the raw material requirements for semiconductor-grade copper–manganese alloy targets.

Keywords: high purity manganese; electrolyte purification; sodium dimethyldithiocarbamate; chemical precipitation; density functional theory

Check for updates

Academic Editor: Sascha Nowak

Received: 19 March 2026
Revised: 6 April 2026
Accepted: 10 April 2026
Published: 18 April 2026

Copyright: © 2026 by the authors. Licensee MDPI, Basel, Switzerland. This article is an open access article distributed under the terms and conditions of the Creative Commons Attribution (CC BY) license.

1. Introduction

Manganese holds an irreplaceable strategic position in fields such as steel metallurgy, energy materials, and semiconductor manufacturing [1–5]. In integrated circuits, as process nodes advance to 28 nm and below, copper interconnect technology faces challenges such as electromigration and RC delay. Copper–manganese alloy thin films have become key materials for deep nanometer node interconnect processes due to their excellent anti-electromigration performance and interfacial stability [6]. The purity of high-purity manganese, which serves as the core raw material for copper–manganese alloy targets,

directly affects the reliability and yield of semiconductor devices; therefore, impurity control in high-purity manganese (>99.999%) used for copper–manganese targets is subject to extremely stringent requirements.

Electrolysis is the primary method for producing high-purity metallic manganese, and product purity depends on the purification degree of the electrolyte [7–10]. Industrial-grade manganese sulfate electrolyte commonly contains impurity ions such as Zn, Ni, Fe, Cr, and Pb, which readily co-deposit with Mn^{2+} during electrodeposition, leading to decreased product purity [11–14]. Developing efficient and highly selective deep purification technologies for electrolytes is the key to solving the technical bottleneck in preparing high-purity manganese for copper–manganese targets.

Heavy metal chelation precipitation has attracted considerable attention in the field of hydrometallurgical purification due to its advantages of high selectivity and simple operation [15,16]. Dithiocarbamate (DTC) chelating agents coordinate with metal ions through sulfur atoms, forming stable five-membered chelate rings, and exhibit excellent capture capability for Cu^{2+}, Zn^{2+}, Pb^{2+}, Cd^{2+}, and other ions [17–20]. Sodium N,N-dimethyldithiocarbamate (sodium dimethyldithiocarbamate, SDD), as a typical small-molecule DTC chelating agent, can rapidly form insoluble complexes under wide pH ranges and ambient temperature conditions, and has been applied in wastewater treatment [21,22]. The two sulfur atoms in the SDD molecule serve as efficient coordination centers due to their low electronegativity (χ = 2.58) and high polarizability; through bidentate coordination with metal ions, five-membered chelate rings are formed, and its selectivity originates from the differences in binding energies of different ions and steric hindrance effects [18]. According to the Hard and Soft Acids and Bases (HSAB) theory, sulfur belongs to soft bases and has a strong affinity for borderline acids and soft acids such as Cu^{2+}, Zn^{2+}, and Pb^{2+} [23]. Mn^{2+} belongs to borderline hard acids due to its larger ionic radius and lower charge density, resulting in poor orbital matching with soft base sulfur atoms; this difference in hard–soft acid–base matching leads to M–S bonds formed between impurity ions and SDD having stronger covalent character and higher thermodynamic stability. Based on this, the effective separation of Mn^{2+} from impurity ions by SDD precipitation is theoretically feasible [15,24–26]. However, systematic studies on the selective deep separation behavior and microscopic coordination mechanisms of multiple impurity ions in manganese sulfate solutions for high-purity electrolytic manganese remain scarce.

This study employs SDD for targeted deep purification of manganese sulfate electrolyte, focusing on solving the challenge of synergistic removal of three key impurity ions: Zn^{2+}, Ni^{2+}, and Pb^{2+}. Combined with density functional theory (DFT) calculations, through analyzing binding energy, electrostatic potential distribution, projected density of states (PDOS), and frontier molecular orbitals, the ligand–metal interaction strength is quantitatively evaluated, and reactive active sites are predicted [18,27], revealing the selective coordination mechanism of major ions in manganese sulfate solution, and elucidating the interaction patterns between sulfur atom active sites and different metal ions at the molecular level, thereby providing theoretical and technical support for achieving deep impurity removal from manganese sulfate solution.

2. Materials and Methods

Industrial electrolytic manganese (Mn $\geq$ 99.5%) was used in the experiments; sulfuric acid (H_2SO_4, analytical grade) and sodium dimethyldithiocarbamate (SDD, $C_3H_6NNaS_2{\cdot}2H_2O$, analytical grade) were used. All water used in the experiments was ultrapure water (resistivity $\geq$ 18.2 MΩ·cm).

2.1. Instruments and Characterization

An inductively coupled plasma mass spectrometer (ICP-MS, Thermo Fisher iCAP RQ, Waltham, MA, USA) was used to determine the concentrations of Mn and trace impurity metal ions in solution, and a glow discharge mass spectrometer (GDMS, Nu Instruments Astrum, Wrexham, UK) was employed to analyze the trace impurity contents in solid metallic manganese samples.

2.2. Experimental Methods

Manganese sulfate solution was prepared using industrial electrolytic manganese. The key parameters of the SDD precipitation process for purifying manganese sulfate solution were investigated to achieve selective and efficient removal of impurity ions from the solution. Finally, electrodeposition experiments were conducted using the purified electrolyte to verify the practical application effect of the purification process. The experimental method is shown in Figure 1.

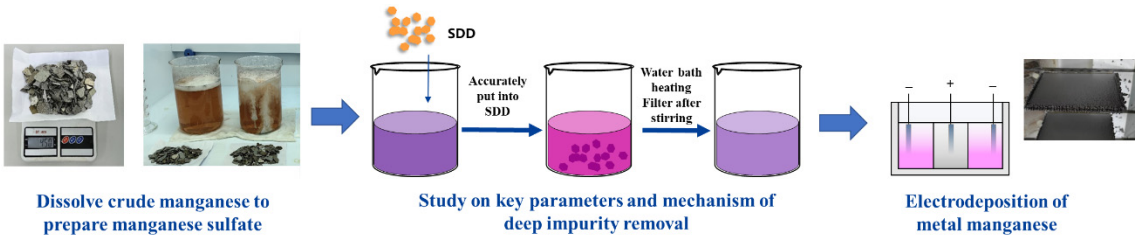


Figure 1. Experimental Methods.

2.2.1. Preparation of Manganese Sulfate Solution

Industrial electrolytic manganese was dissolved in a 1.5 mol/L sulfuric acid solution with a solid-to-liquid ratio of 1:10. After complete dissolution and filtration, the obtained manganese sulfate solution was diluted to obtain a Mn^{2+} concentration of 149.6 g/L. The main components are shown in Table 1.

Table 1. Analysis of main components in the electrolyte before purification (ICP-MS).

Element	Mn	Cr	Cu	Fe	Ni	Pb	Sn	Zn
Content/mg·L^{-1}	149,600	<1.0	<1.0	<0.5	<10.0	<5.0	<2.0	11.8

2.2.2. SDD Precipitation Purification Process

First, 200 mL of the above electrolyte was placed in a 500 mL beaker and heated in a water bath with temperature control. At a certain pH and temperature, a certain amount of sodium dimethyldithiocarbamate was added, and the reaction was carried out with continuous stirring. After the reaction was completed, the mixture was aged at room temperature for 8 h and then filtered under vacuum. The filtrate was collected to determine ion concentrations. The effects of precipitant concentration, reaction temperature, reaction time, and solution pH on impurity removal rate and manganese loss rate were investigated.

2.2.3. DFT Calculation Analysis

The Dmol^3 module was employed to systematically analyze the electronic structure properties of complexes formed by SDD binding with various metal ions, including electrostatic potential distribution, differential charge density, and frontier molecular orbital (HOMO–LUMO) energy levels and distribution.

The generalized gradient approximation (GGA) functional was selected to treat electron exchange–correlation effects, and DFT-D dispersion correction was introduced to

accurately describe van der Waals interactions; core electron effects were treated using DSS semi-core pseudopotentials [28]. During geometry optimization, the self-consistent field (SCF) iteration energy convergence threshold was set to 1.0×10^{-5} Ha, the maximum force convergence threshold between atoms was set to 0.002 Ha/Å, and the maximum atomic displacement convergence threshold was set to 0.005 Å. PDOS calculations employed Gaussian broadening of 0.05 eV; calculations of electrostatic potential distribution and frontier molecular orbital energy levels adopted the same convergence criteria as the ground-state geometry optimization, with calculation accuracy set to Fine level [29].

Upon completion of structural optimization, the binding energy calculation results were utilized to evaluate the thermodynamic stability of each complex and establish the selectivity sequence; geometric parameter statistics were employed to obtain metal–sulfur (M–S) coordination bond length distributions, thereby determining the coordination number and spatial configuration; color-coded three-dimensional electrostatic potential isosurface distribution maps were used for visualization to identify sulfur atom nucleophilic active centers and electron transfer directions; frontier molecular orbital analysis was performed to calculate HOMO–LUMO orbital distributions and energy gaps for correlating the kinetic stability and chemical reactivity of the complexes; deformation density maps were adopted for qualitative analysis of chemical bond composition; and projected density of states (PDOS) calculations were conducted to analyze the energy alignment between metal ion and sulfur electron orbitals and the density of states overlap, quantitatively characterizing orbital hybridization strength.

2.2.4. Electrodeposition Experiment

The purified electrolyte was used as the base catholyte and make-up solution. After adjusting the concentration and pH and incorporating additives, electrodeposition was performed using a stainless steel plate as the cathode and titanium coated with iridium-tantalum as the anode, at a cathodic current density of 400 A/m^2 and a temperature of 40 °C for 24 h. The deposited product was washed, vacuum-dried, and analyzed for purity by GDMS.

3. Results

3.1. Purification Process Conditions of Sodium Dimethyldithiocarbamate (SDD)

In the prepared electrolyte, the contents of zinc, nickel, and lead were 11.8 mg·L^{-1}, <10.0 mg·L^{-1}, and <5.0 mg·L^{-1}, respectively. Due to the reduction potentials of these three impurities being close to that of Mn^{2+}, they readily co-deposit with manganese during electrodeposition, affecting the purity and compactness of the deposited layer; therefore, they must be strictly removed [12,30,31]. The effects of various process parameters were investigated through experiments.

3.1.1. Effect of SDD Precipitant Concentration

To investigate the effect of precipitant concentration on impurity removal, precipitation experiments were conducted using SDD at concentrations of 0.25, 0.5, 1, 5, and 10 g/L, with solution pH controlled at 6.5, reaction temperature at 55 °C, reaction time of 2 h, and aging at room temperature for approximately 8 h after reaction. The results are shown in Figure 2.

As SDD concentration increased from 0.25 g/L to 1 g/L, the removal efficiency of the three characteristic impurity ions improved significantly with increasing SDD dosage, wherein the concentration of Zn^{2+} in the solution decreased from 8.21 mg/L to 0.065 mg/L, Ni^{2+} from 1.62 mg/L to 0.13 mg/L, and Pb^{2+} from 0.92 mg/L to 0.07 mg/L. Meanwhile, the Mn^{2+} concentration decreased from 145.3 g/L to 132.4 g/L. When SDD concentration con-

tinued to increase to 10 g/L, no further reduction in impurity concentrations was observed (Zn^{2+} 0.12 mg/L, Ni^{2+} 0.18 mg/L, and Pb^{2+} 0.05 mg/L), while the Mn^{2+} concentration decreased to 130.7 g/L. An appropriate precipitant concentration can improve impurity removal efficiency; however, excessive SDD concentration did not further improve impurity removal but increased co-precipitation loss with Mn^{2+}. Considering both removal efficiency and manganese co-precipitation loss, the optimal SDD dosage concentration was determined to be 1 g/L, ensuring complete complexation of impurities while minimizing manganese loss to the greatest extent.

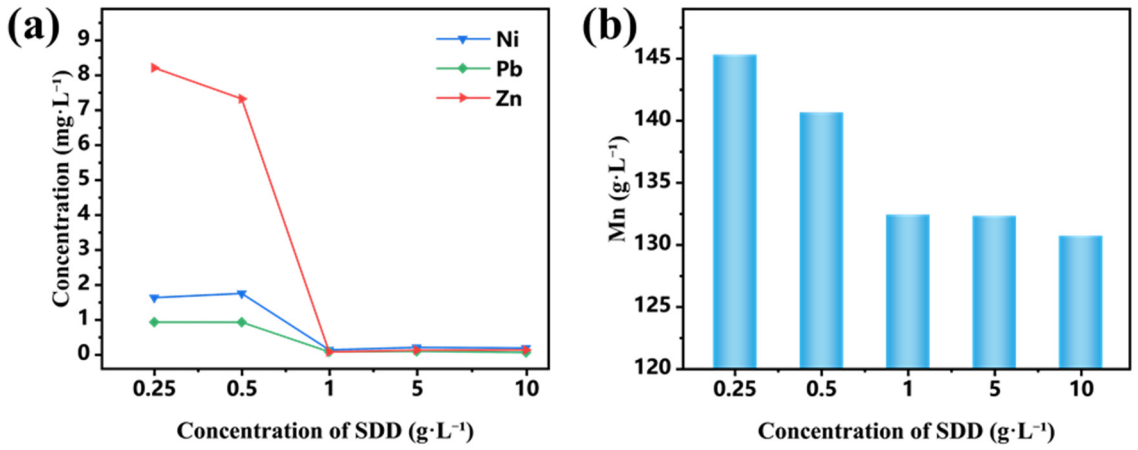


Figure 2. Effect of precipitant concentration on (**a**) impurity content and (**b**) manganese content.

3.1.2. Effect of Reaction Temperature

To investigate the effect of reaction temperature on impurity removal, precipitation experiments were conducted at different temperatures (25 °C, 45 °C, 55 °C, 65 °C, and 75 °C) with a precipitant concentration of 1 g/L, solution pH of 6.5, and reaction time of 2 h, followed by aging at room temperature for approximately 8 h. The experimental results are shown in Figure 3.

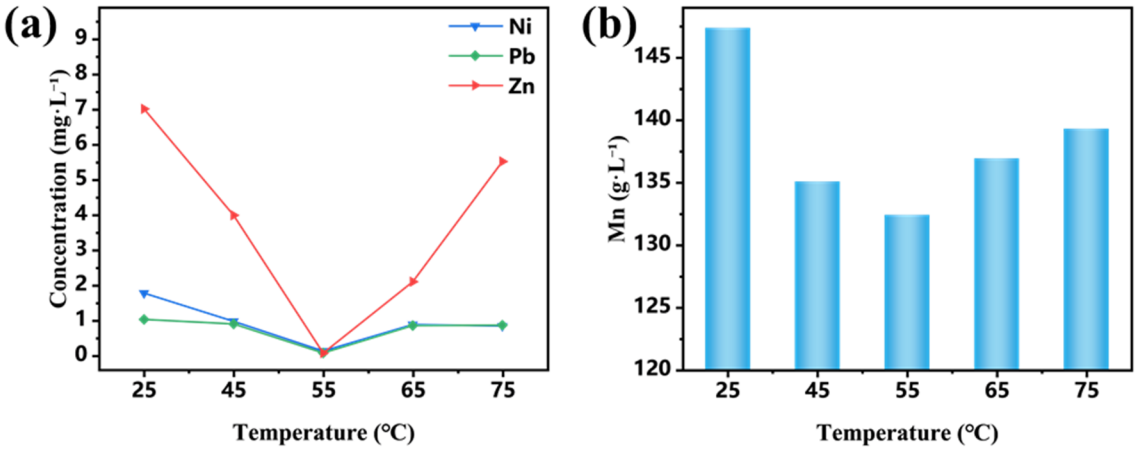


Figure 3. Effect of reaction temperature on (**a**) impurity content and (**b**) manganese content.

Within the temperature range of 25–55 °C, the removal efficiency of the three impurity ions improved with increasing temperature, wherein the Zn^{2+} concentration decreased from 7.02 mg/L to 0.065 mg/L, Ni^{2+} from 1.78 mg/L to 0.13 mg/L, and Pb^{2+} from 1.02 mg/L to 0.07 mg/L; the Mn^{2+} concentration decreased from 147.4 g/L to 132.4 g/L. Appropriate heating can promote effective contact between SDD molecules and metal ions and enhance

the kinetics of chelation reactions, while reducing solution viscosity, which favors the aggregation and settling of precipitates.

When the temperature exceeded 55 °C, the Zn^{2+} concentration rebounded to 2.10 mg/L (at 65 °C) and 5.52 mg/L (at 75 °C), and the concentrations of Ni^{2+} and Pb^{2+} also increased significantly, while the Mn^{2+} concentration was 139.3 g/L at 75 °C, higher than that at 55 °C. Dialkyldithiocarbamates possess certain thermal stability in alkaline solutions, but elevated temperatures may accelerate the oxidation of SDD to thiuram disulfide, leading to a decrease in effective ligand concentration [32]; meanwhile, higher temperatures may alter the solubility equilibrium of metal–DTC complexes, causing partial dissociation or redissolution of the formed chelates [33]. Therefore, the optimal reaction temperature was determined to be 55 °C.

3.1.3. Effect of Reaction Time

To investigate the effect of reaction time on impurity removal, precipitation experiments were conducted with an SDD precipitant concentration of 1 g/L, a reaction temperature of 55 °C, and a solution pH of 6.5, setting reaction times of 0.5 h, 1 h, 1.5 h, 2 h, and 3 h, followed by aging at room temperature for approximately 8 h. The experimental results are shown in Figure 4.

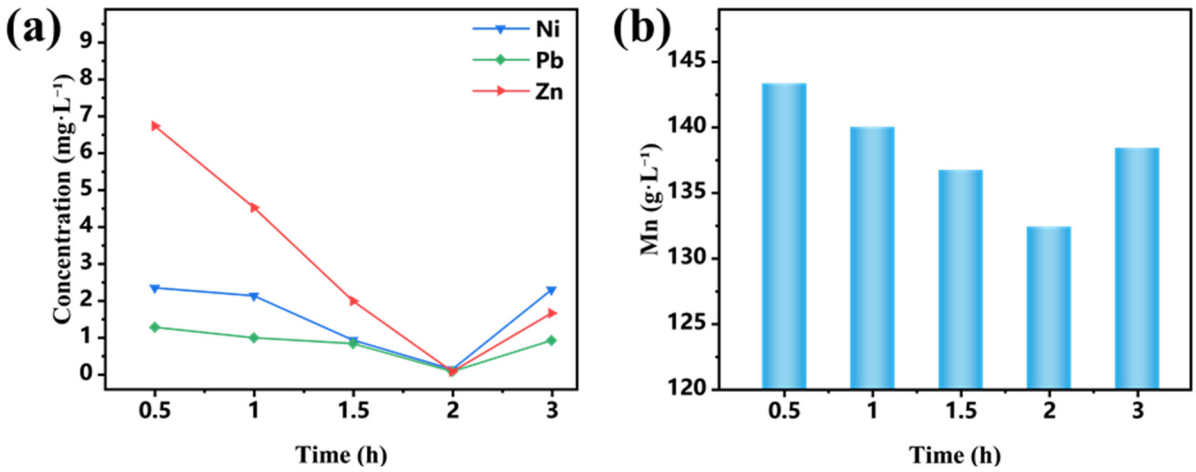


Figure 4. Effect of reaction time on (**a**) impurity content and (**b**) manganese content.

Within the reaction time of 0.5–2 h, the Zn^{2+} concentration in solution decreased from 6.73 mg/L to 0.065 mg/L, Ni^{2+} from 2.34 mg/L to 0.13 mg/L, and Pb^{2+} from 1.27 mg/L to 0.07 mg/L; the Mn^{2+} concentration decreased from 140.3 g/L to 132.4 g/L. Sufficient mass transfer time ensured effective contact between SDD molecules and metal ions and complete chelation reaction. After a reaction time of 2 h, the impurity concentrations reached minimum values (Zn^{2+} 0.065 mg/L, Ni^{2+} 0.13 mg/L, and Pb^{2+} 0.07 mg/L).

When the reaction time was extended to 3 h, the impurity ion concentrations showed significant rebound (Zn^{2+} increased to 1.65 mg/L, Ni^{2+} to 2.29 mg/L, and Pb^{2+} to 0.91 mg/L), while the Mn^{2+} concentration increased to 138.4 g/L. DTC-metal complexes exist in coordination–dissociation equilibrium in the solution; prolonged stirring may destroy floc structure or promote transformation of complexes to more stable forms; and extending reaction time also increases the opportunity for SDD oxidation, which may cause partial oxidation of DTC to thiuram disulfide and subsequent deactivation [32]. Therefore, the optimal reaction time was determined to be 2 h.

3.1.4. Effect of Solution pH

To investigate the effect of pH on impurity removal, precipitation experiments were conducted under the conditions of a precipitant concentration of 1 g/L, a reaction temperature of 55 °C, and a reaction time of 1 h, controlling the solution pH at 3.5, 5.5, 6.5, 7.5, and 7.75, followed by aging at room temperature for approximately 8 h after the reaction. The experimental results are shown in Figure 5.

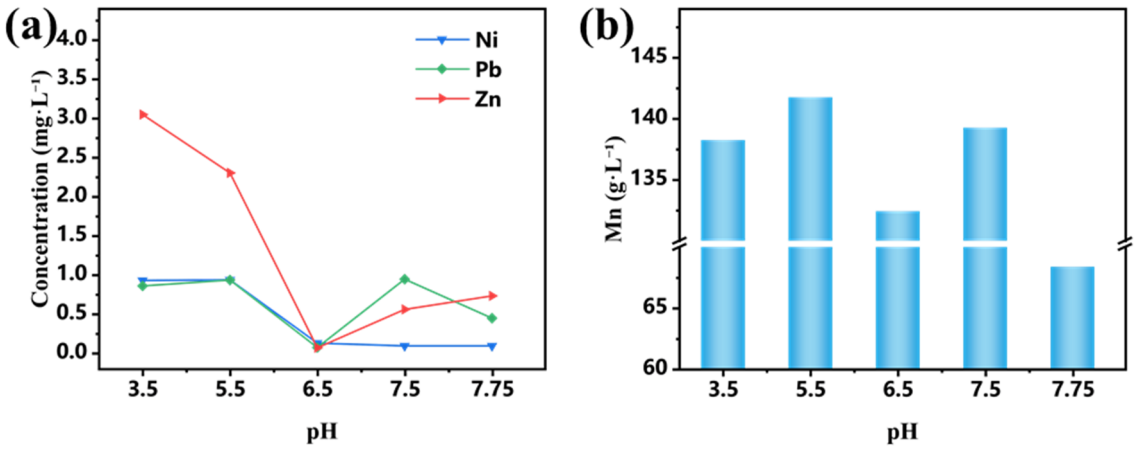


Figure 5. Effect of solution pH on (**a**) impurity content and (**b**) manganese content.

The pH value has a significant effect on the removal of impurity metal ions. When pH increased gradually from 3.5 to 6.5, the Zn^{2+} concentration decreased from 3.05 mg/L to 0.065 mg/L, Ni^{2+} from 0.93 mg/L to 0.13 mg/L, and Pb^{2+} from 0.86 mg/L to 0.07 mg/L; the Mn^{2+} concentration decreased from 138.2 g/L to 132.4 g/L. In acidic media, the anionic form of DTC (-CSS^-) is rapidly protonated to form unstable dithiocarbamic acid (-CSSH), decomposing to produce amine and carbon disulfide [32]; this protonation significantly reduces the electron-donating ability of the coordinating sulfur atoms, leading to decreased chelating ability. At pH 6.5, the purification effect was optimal, and the concentrations of the three key impurity ions all decreased to the minimum.

When pH further increased to 7.5, the concentrations of Zn^{2+} and Pb^{2+} rebounded (increasing to 0.56 mg/L and 0.94 mg/L, respectively). When pH increased to 7.75, the Mn^{2+} concentration dropped sharply to 68.4 g/L, while the impurity removal effect was also poor (Zn^{2+} 0.73 mg/L, Ni^{2+} 0.09 mg/L, and Pb^{2+} 0.44 mg/L). Under high pH conditions, OH^- competes with DTC for coordination, possibly forming soluble hydroxo complexes or destroying the stability of DTC-metal chelates [34]; meanwhile, high pH promotes the direct hydrolysis of Mn^{2+} to form $Mn(OH)_2$ precipitate. Therefore, the optimal pH was determined to be 6.5.

In summary, under the optimized conditions of a precipitant concentration of 1 g/L, a solution pH of 6.5, a reaction temperature of 55 °C, and a reaction time of 2 h, purification treatment was conducted. The composition of the purified electrolyte is shown in Table 2. After purification, the concentrations of the three key impurity ions in the solution were Zn 0.07 mg/L, Ni 0.13 mg/L, and Pb 0.07 mg/L, demonstrating a significant deep impurity removal effect. The Mn^{2+} concentration was 142.6 g/L, which was slightly decreased.

Table 2. Composition of the electrolyte after purification under optimized conditions.

Element	Mn	Cr	Cu	Fe	Ni	Pb	Sn	Zn
Content/mg·L^{-1}	142,680	0.06	0.01	0.07	0.13	0.08	0.02	0.07

3.2. Theoretical Analysis of Selective Impurity Removal by Sodium Dimethyldithiocarbamate

3.2.1. Binding Energy Calculation

To validate the simplified DFT model under experimental conditions, aqueous speciation calculations were performed using the Medusa chemical equilibrium software (https://www.kth.se/che/medusa, accessed on 9 April 2026) with the inherent thermodynamic database. Figure S1 confirms that at the optimized pH of 6.5, Zn^{2+}, Ni^{2+}, and Mn^{2+} exist almost exclusively as free aqua ions (>98%), while Pb^{2+} is present predominantly as Pb^{2+} (~95%) with minor $PbOH^{+}$ (~5%). This validates the DFT model employing bare M^{2+} ions as the reactive species. Density functional theory (DFT) calculations were performed using the DMol3 module, and the binding energies (ΔE) between SDD and the target ion Mn^{2+}, as well as impurity ions (Zn^{2+}, Ni^{2+}, and Pb^{2+}), were systematically calculated. The binding energy calculation formula is as follows:

$$\Delta E = E_{M[SDD]} - (E_M + E_{SDD}) \quad (1)$$

where $E_{M[SDD]}$ is the total energy of the metal–SDD complex, E_M is the energy of the metal ion, and E_{SDD} is the energy of the SDD molecule. The calculation results are shown in Table 3.

Table 3. Binding energy calculation of metal–SDD complexes (kcal/mol).

	$E_{M[SDD]}$	E_{SDD}	E_M	ΔE
Mn	-1.94×10^6	-1.22×10^6	-7.22×10^5	−221.70
Zn	-2.33×10^6	-1.22×10^6	-1.12×10^6	−271.81
Ni	-2.16×10^6	-1.22×10^6	-9.46×10^5	−372.40
Pb	-1.35×10^7	-1.22×10^6	-1.23×10^7	−297.94

The order of absolute values is: Ni^{2+} (−372.40 kcal/mol) > Zn^{2+} (−271.81 kcal/mol) > Pb^{2+} (−297.94 kcal/mol) > Mn^{2+} (−221.70 kcal/mol). This ordering indicates that significant differences exist in the affinity of SDD for the four ions; the complex formed by Ni^{2+} with SDD exhibits the highest thermodynamic stability, whereas the binding ability of Mn^{2+} with SDD is the weakest.

The binding energy difference among the four ions exceeds 50 kcal/mol. This energy gradient ensures that in a competitive coordination system, SDD will preferentially bind with Zn^{2+}, Ni^{2+}, and Pb^{2+}, providing a thermodynamic foundation for the selective purification of the Mn^{2+} solution.

3.2.2. Coordination Geometry and Electrostatic Potential Distribution Characteristics

Geometric structure optimization was performed using density functional theory (DFT) calculations, and the geometric configurations are shown in Figure 6. The results indicate that all metal ions form four-coordinate structures with four sulfur atoms from two SDD molecules. However, specific differences exist in the spatial arrangement of ligands induced by different metal ions: in Mn^{2+}, Zn^{2+}, and Ni^{2+} complexes, the two SDD ligand molecules exhibit an approximately perpendicular spatial arrangement (dihedral angle ~90°), forming a distorted tetrahedral coordination configuration, whereas in the Pb^{2+} complex, the two SDD molecules are essentially coplanar (dihedral angle ~0°), forming a planar quadrilateral configuration.

As shown in Table 4, the metal–sulfur coordination bond lengths (M–S) exhibit a regular sequence: the average coordination distance of Ni^{2+} is the shortest (2.306 Å), that of Zn^{2+} is 2.383 Å, that of Mn^{2+} is 2.431 Å, and due to its largest ionic radius, Pb^{2+} has an average coordination distance of 2.791 Å.

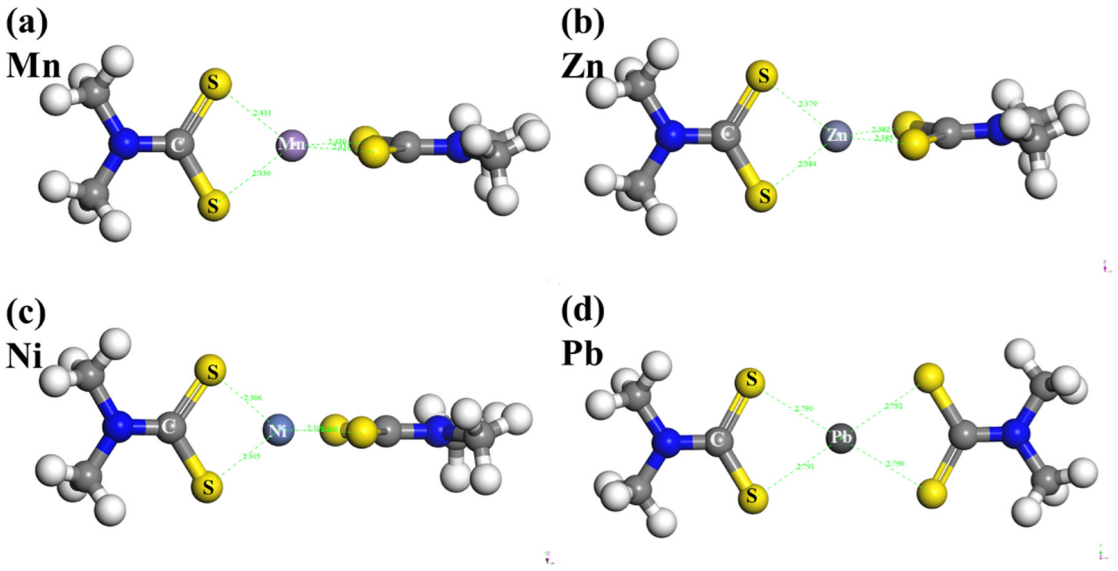


Figure 6. Complex structures of SDD molecules with (**a**) Mn, (**b**) Zn, (**c**) Ni, and (**d**) Pb after structural optimization.

Table 4. Distribution of M–S coordination bond lengths after structural optimization.

Element	Distance 1 (Å)	Distance 2 (Å)	Distance 3 (Å)	Distance 4 (Å)	Average Distance (Å)
Mn	2.431	2.430	2.430	2.431	2.431
Zn	2.379	2.384	2.382	2.385	2.383
Ni	2.306	2.305	2.306	2.305	2.306
Pb	2.790	2.791	2.792	2.790	2.791

In metal–ligand complexes, the degree of electron delocalization directly reflects the covalent character of the metal–ligand bond: highly delocalized electron distributions (electron cloud distributions extending to regions between multiple nuclei) correspond to strong covalent interactions, whereas localized electron distributions (electron clouds primarily distributed in spatial regions around specific nuclei) correspond to ionic or weak interactions [25]. Electrostatic potential (ESP) distribution maps display the spatial distribution characteristics of electron density on molecular surfaces through color coding (red regions indicate electron enrichment with negative electrostatic potential; blue regions indicate electron deficiency with positive electrostatic potential). As shown in Figure 7, the electrostatic potential distributions of complexes formed by different metal ions with SDD exhibit systematic differences.

In the Ni^{2+} complex (Figure 7c), the metal center region exhibits an obvious blue positive electrostatic potential, indicating relatively low electron density in this region. This phenomenon arises from the overlap of Ni^{2+} d-orbital electrons with lone pair electrons of the ligand sulfur atoms during strong covalent bond formation; the electron cloud transfers from the region surrounding the metal nucleus to the Ni–S bond region, resulting in reduced local electron density at the metal center, reflecting the electron rearrangement characteristics of covalent bonds.

The metal center of the Pb^{2+} complex exhibits a deep red negative electrostatic potential under the same scale (Figure 7d), indicating significantly higher electron density around it than that of the Ni^{2+} center. This is consistent with the $6s^2$ inert electron pair structure of Pb^{2+}: during bond formation, the 6s electrons are difficult to fully participate in orbital overlap and partially remain localized near the metal atom, rendering the metal–ligand interaction partially localized; meanwhile, the planar configuration of the complex results

in axial asymmetry of its electrostatic potential, with electron density distribution being more diffuse along the direction perpendicular to the ligand plane.

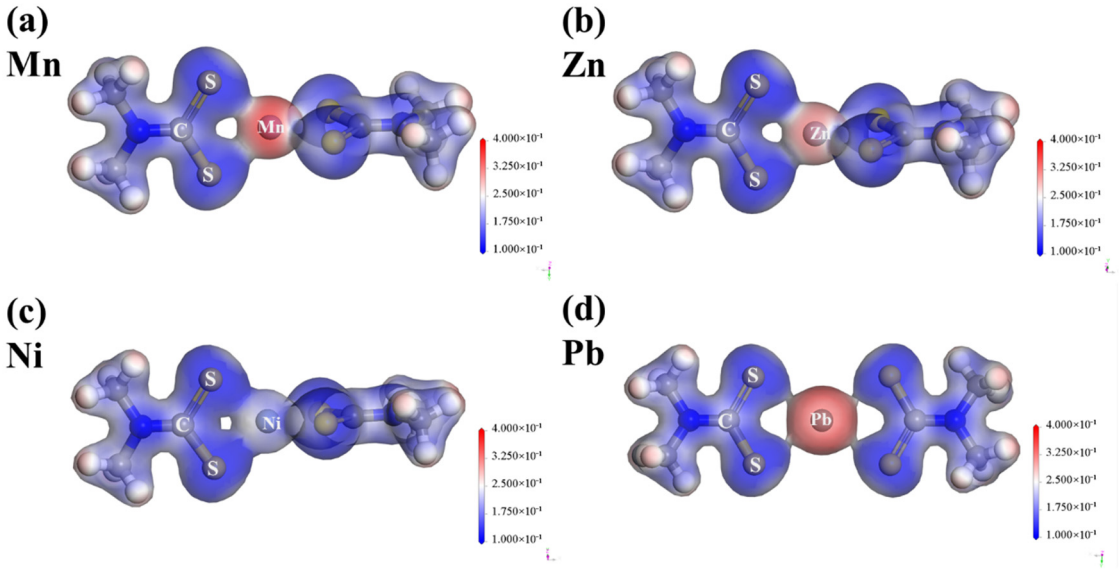


Figure 7. Electrostatic potential distribution maps of metal–SDD complexes.

Mn^{2+} and Zn^{2+} exist in a transitional state between the above two modes (Figure 7a,b): the relatively high electron density at the Mn center corresponds to long bond length and low binding energy, indicating weak bonding interaction and limited electron cloud rearrangement; the electron density at the Zn center is lower than that of Mn, displaying a certain degree of electron transfer, with its covalency being higher than Mn but weaker than Ni, which is consistent with the previously described characteristics of Zn having medium bond length and binding energy.

3.2.3. Frontier Molecular Orbitals and Reactivity Characteristics of Metal–SDD Complexes

Frontier molecular orbital analysis reveals significant differences in HOMO–LUMO energy gaps among different metal–SDD complexes, corresponding to different chemical reactivities (Figure 8). The calculated energy gap values follow the order: Pb^{2+} (−0.493 eV) < Ni^{2+} (−0.723 eV) < Mn^{2+} (−1.751 eV) < Zn^{2+} (−3.530 eV).

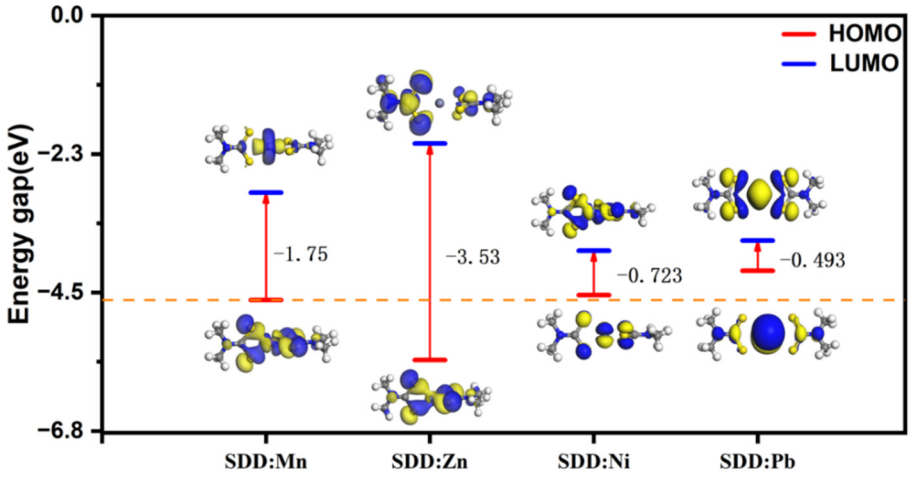


Figure 8. Frontier orbital energy levels and energy gaps of metal–SDD complexes.

According to frontier molecular orbital theory, the smaller the absolute value of the energy gap, the easier the electron transition and the higher the chemical reactivity. Pb^{2+}

and Ni^{2+} complexes exhibit smaller absolute energy gap values (0.493 eV and 0.723 eV), indicating lower energy barriers for electron transition from HOMO to LUMO, higher chemical reactivity, and favorable conditions for rapid nucleation; the Zn^{2+} complex possesses the largest absolute energy gap value (3.530 eV), exhibiting greater resistance to electron transfer and the lowest reactivity; and Mn^{2+} lies between the two (1.751 eV), with moderate complex stability but insufficient kinetic activity.

3.2.4. Deformation Charge Density and Bonding Characteristics

Deformation charge density analysis (Δρ) intuitively presents the electron redistribution during the bonding process by calculating the difference in electron density between the complex and isolated atoms (Figure 9).

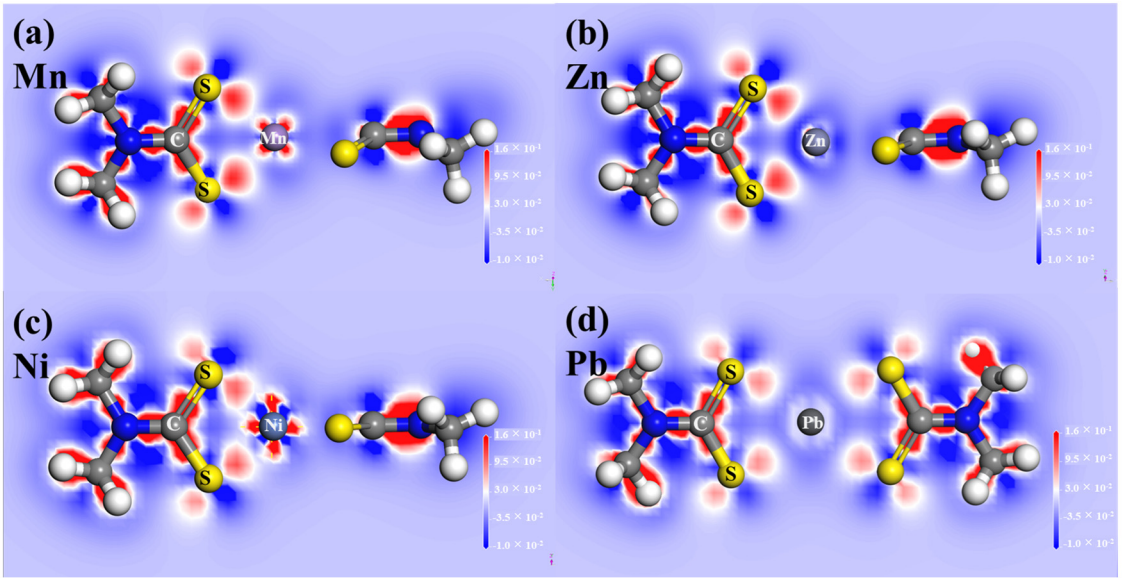


Figure 9. Deformation charge density maps of metal–SDD complexes (Δρ).

In the Mn–SDD system (Figure 9a), the electron accumulation in the bond region appears as rounded "water-drop-like" shapes, with diffuse electron cloud distribution and low overlap degree along the bond axis, reflecting weak covalent interactions consistent with its long bond length of 2.431 Å and low binding energy characteristics.

The Zn–SDD system (Figure 9b) shows clearly bounded "triangular" electron accumulation lobes, with directional aggregation of electron cloud in the bond region, indicating enhanced orbital overlap and the formation of medium-strength σ bonds.

The Ni–SDD system (Figure 9c) exhibits significantly extended distribution ranges of electron accumulation lobes, extending from the bond region to the interior of the metal center and displaying sheet-like delocalization characteristics. This indicates that Ni d-electrons conjugate with sulfur atom p-orbitals, forming a highly delocalized electron system, corresponding to its shortest bond length of 2.306 Å and highest binding energy.

The Pb–SDD system (Figure 9d) presents light red electron accumulation in the S–Pb bond region, while electron cloud bridging is observed between the two SDD ligands. This cross-ligand electron delocalization is related to the coplanar configuration, indicating the existence of lateral p–p orbital interactions that compensate for the energy loss caused by long bonds.

3.2.5. Projected Density of States (PDOS) Calculation

The projected density of states (PDOS) of metal ions and sulfur atoms in the complexes was calculated to further quantitatively elucidate the electronic structure differences

observed in the deformation density, as shown in Figure 10. In the figure, the s, p, and d curves represent the projected density of states for the s, p, and d valence electron orbitals of each atom, respectively.

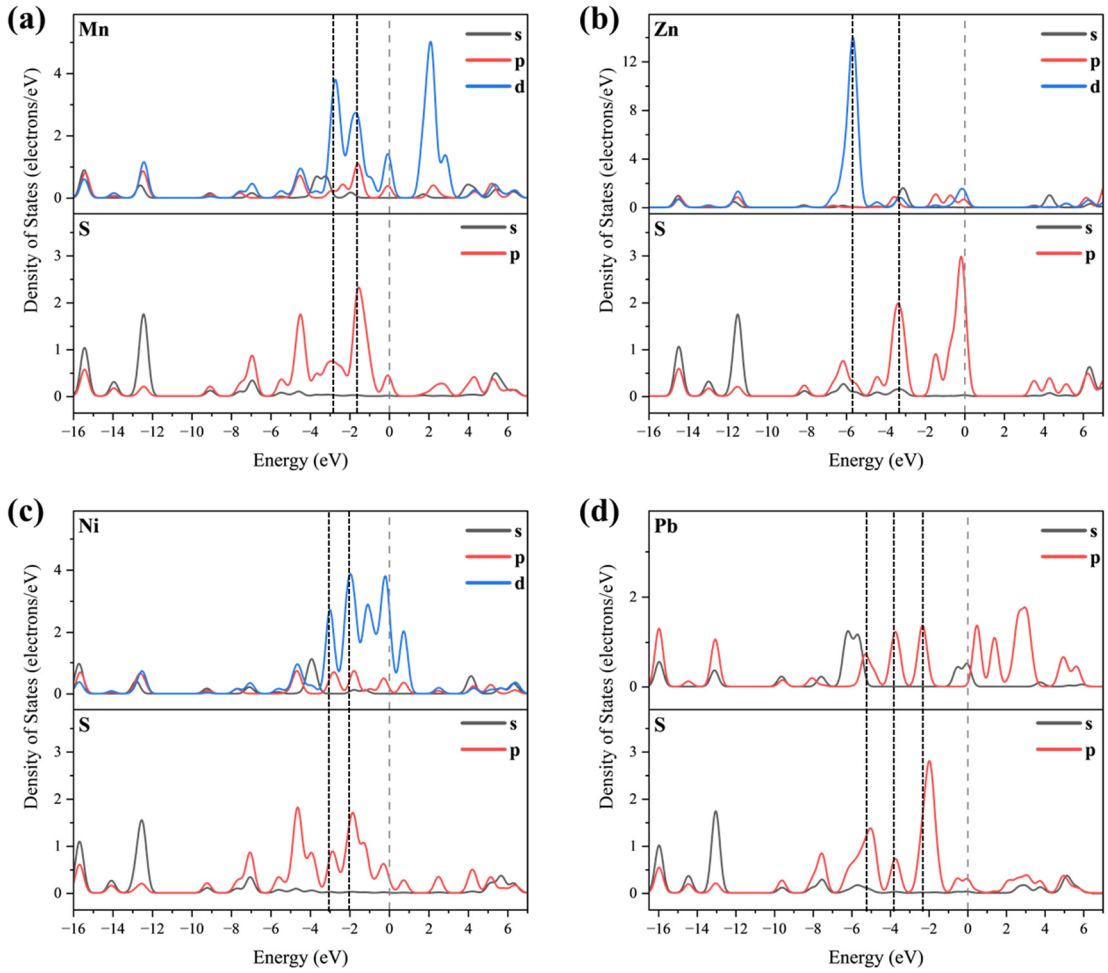


Figure 10. Projected density of states (PDOS) of metal ions (**a**) Mn, (**b**) Zn, (**c**) Ni, and (**d**) Pb and coordinating sulfur atoms.

The PDOS of Ni^{2+} displays multiple strong resonance peaks in the occupied state region. The strongest occupied state peak is located at −1.96 eV, almost perfectly aligned with the main p-orbital peak of the ligand S at −1.83 eV (ΔE = 0.13 eV), forming the first resonance pair; the secondary occupied state peak at −2.99 eV forms a second resonance pair with the ligand S p-orbital at −2.86 eV (ΔE = 0.13 eV). Of particular importance, a high-density state peak exists near the Fermi level (−0.19 eV, accounting for 98.2% of the main peak), forming a third resonance pair with the ligand S p-orbital at −0.28 eV (ΔE = 0.09 eV). This orbital overlap near the Fermi level endows the Ni–SDD complex with high reactivity, while a significant peak exists in the unoccupied states at 0.75 eV, facilitating electron acceptance. The d-band center of Ni is located at −2.79 eV, exhibiting high energy matching with the p-band center of the ligand S, forming a multicenter resonance system that quantitatively explains the highly delocalized electron phenomenon and the highest binding energy observed in the deformation density.

PDOS analysis of Pb^{2+} reveals the existence of dual strong orbital resonances between Pb^{2+} and ligand S. Within the energy range of −7 to −1 eV, the 6p orbital of Pb^{2+} presents three significant peaks, two of which form strong energy alignments with ligand S: the first resonance pair is located at Pb (−5.29 eV) and ligand S (−5.02 eV), with an energy difference

of only 0.27 eV; the second resonance pair is located at Pb (−2.33 eV) and S (−1.97 eV), with an energy difference of 0.36 eV. Both resonance pairs exhibit energy differences smaller than 0.5 eV, falling within the range of strong orbital overlap. This indicates that the Pb–S bond possesses significant covalent character. Pb^{2+} exhibits a prominent peak at −3.73 eV (DOS reaching 1.2289), corresponding to the localized characteristic of the $6s^2$ inert electron pair. The ligand S also presents a minor peak (DOS < 1) near this energy, forming a third weak resonance pair with the Pb peak. However, since the intensity of the S peak is only approximately 50–80% of that of the Pb peak, the degree of orbital overlap is limited, and this peak primarily originates from $6s^2$ electrons that are difficult to participate in bonding; therefore, this interaction contributes weakly to the covalency of the Pb–S bond, mainly reflecting the electron localization characteristic at the metal center. This reflects the $6s^2$ inert electron pair effect of Pb^{2+}: partial 6s electrons are localized near the metal center and are difficult to participate in bonding. This dual characteristic of being partially bonding and partially localized enables the Pb–SDD complex to possess high thermodynamic stability while retaining ionic character, and explains its longer coordination bond length (2.791 Å)—multiple orbital overlaps compensate for the disadvantage of distance, forming a stable multicenter coordination structure.

The d-orbital of Zn^{2+} exhibits a typical d^{10} full-shell distribution, with the main peak located at −5.65 eV and the band center at −5.95 eV. A secondary peak of the ligand S p-orbital exists at −6.15 eV, with an energy difference of only 0.50 eV from the main peak of Zn^{2+}, forming a weak orbital resonance. However, this resonance is limited by two factors: first, the d-orbitals of Zn^{2+} are fully occupied, and the density of states near the Fermi level (in the region of −0.16 eV to 0.01 eV) approaches zero, lacking effective electron acceptor orbitals; second, the spherical symmetry of the d^{10} configuration results in inefficient orbital overlap. Although weak energy alignment exists near −6 eV, the orbital overlap integral between Zn^{2+} and ligand S near the Fermi level is only 15.2% of that in the Ni^{2+} system, confirming that the interaction remains electrostatically dominated with a limited covalent component.

Mn^{2+} exhibits typical characteristics of a d^5 high-spin configuration. The main peak of the occupied states is located at −2.71 eV, exhibiting weak resonance with the secondary peak of the ligand S p-orbital at −2.88 eV (ΔE = 0.17 eV); the secondary peak at −1.68 eV forms a second weak resonance with the main peak of the ligand S p-orbital at −1.54 eV (ΔE = 0.14 eV). However, compared with Ni^{2+}, the density of states of Mn^{2+} near the Fermi level (−0.06 eV) is lower (only 28.1% of the main peak), and its unoccupied state main peak is located at 2.11 eV, distant from the occupied orbitals of ligand S. The d-band center of Mn is located at −4.11 eV, exhibiting poor energy matching with the p-orbitals of ligand S; this orbital energy mismatch, together with the spherical symmetric distribution of d-electrons, collectively leads to weak electrostatic interaction.

The above calculation results collectively elucidate the selective impurity removal mechanism of SDD from three dimensions: thermodynamics, kinetics, and electronic structure.

From the thermodynamic dimension, the binding energy sequence (Ni^{2+} > Pb^{2+} > Zn^{2+} > Mn^{2+}) with differences exceeding 50 kcal/mol indicates that SDD preferentially forms stable complexes with impurity ions. From the kinetic dimension, the frontier orbital energy gaps (smaller for Ni^{2+} and Pb^{2+}, larger for Mn^{2+} and Zn^{2+}) correspond to impurity ion complexes possessing higher chemical reactivity and faster precipitation kinetics.

From the electronic structure dimension, PDOS, deformation density, and electrostatic potential analyses present consistent differences in bonding characteristics: Ni^{2+} forms strong covalent bonds through d–p resonance; Pb^{2+} forms delocalized π interactions through in-plane matching of 6p orbitals, with its coplanar configuration (different from the perpendicular configurations of Mn/Zn/Ni) optimizing orbital overlap; Zn^{2+} relies on

electrostatic attraction of the d^{10} full shell; and Mn^{2+}, due to orbital dispersion and energy mismatch of the d^5 high-spin configuration, forms the weakest electrostatic interaction. These electronic structure differences are interrelated with geometric configuration characteristics (bond length and ligand orientation), collectively constituting the theoretical foundation for the selective separation of impurity ions from Mn^{2+} in manganese sulfate solution by SDD.

3.3. Electrodeposition of Purified Solution

The obtained purified solution was used as the electrolyte. The Mn concentration was diluted to 19 g/L, ammonium sulfate was supplemented to 110 g/L, and 0.02 g/L Na_2SO_3 was added as an additive, after which constant current electrodeposition experiments were conducted. A titanium plate (100 mm × 100 mm) was used as the cathode, and a titanium coated with iridium-tantalum material was used as the anode; the electrode spacing was 3 cm, the cathodic current density was 400 A/m^2, the temperature was controlled at 40 ± 1 °C, and electrolytic deposition was carried out for 24 h. After completion of the electrolytic deposition, the cathode product was rinsed with ultrapure water and dried in a vacuum drying oven at 60 °C for 4 h. The obtained metallic manganese was subjected to full elemental analysis using glow discharge mass spectrometry (GDMS), and the analysis results are shown in Table 5. The zinc content was 0.11 mg/kg, the nickel content was 0.038 mg/kg, the iron content was 0.19 mg/kg, the chromium and copper contents were 0.012 mg/kg and 0.099 mg/kg, respectively, and the lead content was less than 0.05 mg/kg. The total sulfur content in the electrodeposited manganese was determined to be 0.72 mg/kg (Table 5), confirming that SDD-derived sulfur was effectively removed during the purification process and did not contaminate the final product.

Table 5. GDMS analysis results of the main impurity elements in the electrodeposited manganese product.

Element	Measured Result (mg/kg)	Element	Measured Result (mg/kg)	Element	Measured Result (mg/kg)
Li	<0.005	Ga	<0.05	Nd	<0.005
Be	<0.005	Ge	<0.05	Sm	<0.005
B	0.049	As	<0.05	Eu	<0.005
Cu	0.099	Se	<0.5	Gd	/
Zn	0.11	Br	<0.5	Tb	<0.005
Ni	0.038	Rb	<0.05	Dy	<0.005
F	0.081	Sr	/	Ho	/
Na	0.72	Y	/	Er	<0.005
Mg	0.073	Zr	<0.05	Tm	<0.005
Al	0.072	Nb	0.60	Yb	<0.005
Si	1.09	Mo	<0.05	Lu	<0.005
P	0.021	Ru	<0.05	Hf	<0.05
S	0.72	Rh	<0.05	Ta	0.14
Cl	/	Pd	<0.05	W	<0.5
K	1.40	Ag	0.067	Rc	<0.5
Ca	0.23	Cd	<0.05	Os	<0.05
Sc	<0.005	In	<0.05	Ir	<0.05
Ti	0.019	Sn	0.13	Pt	<0.05
V	<0.005	Sb	<0.05	Au	<0.05
Cr	0.012	Te	<0.05	Hg	<0.05
Mn	base	I	<0.05	Tl	<0.05
Fe	0.19	Cs	<0.05	Pb	<0.05
Co	0.10	Ba	<0.05	Bi	<0.05
Pr	<0.005	La	<0.005	Th	<0.005
Ce	<0.005	U	<0.005		

GDMS full elemental analysis indicates that after SDD purification treatment, the manganese sulfate electrolyte can meet the requirements for preparing semiconductor-grade high-purity manganese, and the prepared electrolytic metallic manganese product achieves a purity above 99.999%, satisfying the raw material requirements for copper–manganese alloy targets.

4. Conclusions

This study addresses the challenge of deep removal of three key impurity ions (zinc, nickel, and lead) during the electrodeposition of high-purity manganese, successfully preparing metallic manganese products with purity reaching 5N (99.999%) and above, and investigates the purification process of manganese sulfate electrolyte based on sodium dimethyldithiocarbamate chelation precipitation. The main conclusions are as follows:

(1) The optimal process parameters were determined: precipitant concentration of 1 g/L, solution pH of 6.5, reaction temperature of 55 °C, and reaction time of 2 h. Under these conditions, the concentrations of Zn, Ni, and Pb in the electrolyte were reduced to 0.07 mg/L, 0.13 mg/L, and 0.08 mg/L, respectively, achieving efficient synergistic removal of the three impurities.

(2) Density functional theory calculations elucidated the selectivity mechanism from the perspectives of thermodynamics, kinetics, and electronic structure. Thermodynamically, the absolute values of binding energies follow the order Ni > Pb > Zn > Mn, indicating that SDD possesses higher coordination stability with impurity ions. Kinetically, frontier orbital energy gap analysis reveals that Pb and Ni exhibit higher reactivity, whereas the complexes of Mn and Zn have larger energy gaps and relatively lower kinetic activity. Electronic structure and geometric configuration analyses corroborate these findings. These multidimensional factors collectively constitute the theoretical foundation for the selective preferential coordination of SDD with impurity ions (Ni, Pb, and Zn) rather than Mn^{2+}.

(3) Electrodeposition experiments of the purified solution indicate that, in the electrolytic metallic manganese obtained, the contents of Zn, Ni, and Pb are 0.11 mg/kg, 0.038 mg/kg, and <0.05 mg/kg, respectively, and the manganese purity reaches above 99.999%, satisfying the raw material requirements for copper–manganese alloy targets used in semiconductors.

Supplementary Materials: The following supporting information can be downloaded at: https://www.mdpi.com/article/10.3390/separations13040123/s1, Figure S1. Species distribution diagrams of (a) Mn, (b) Zn, (c) Ni, and (d) Pb as a function of pH, calculated using Medusa software (25 °C). The vertical dashed line indicates the experimental pH (6.5), where all metal ions exist predominantly (>95%) as free M^{2+} aqua ions, validating the simplified DFT model.

Author Contributions: Software, K.H.; Formal analysis, F.Z.; Investigation, T.L. and X.T.; Resources, K.H.; Writing—original draft, T.L.; Writing—review & editing, F.Z., X.T., Z.C. and S.C.; Supervision, F.Z., Z.C. and S.C.; Project administration, S.C.; Funding acquisition, S.C. All authors have read and agreed to the published version of the manuscript.

Funding: This research was funded by Innovation Fund of China GRINM Technology Group grant number JT61061002501.

Data Availability Statement: Data is contained within the article or Supplementary Material.

Conflicts of Interest: The authors declare that they have no known competing financial interests or personal relationships that could have appeared to influence the work reported in this paper. Authors Fei Zhu, Zhenping Cai, and Song Chen were employed by the company GRINM Resources and Environment Tech. Co., Ltd., Beijing 100088, China. Authors Tong Liu and Xijun Tian were graduate

students (not formal employees) at the General Research Institute for Nonferrous Metals (GRINM), and were affiliated with and managed by the GRINM Environmental Protection Engineering Research Institute and the China GRINM Technology Group. The remaining authors declare that the research was conducted in the absence of any commercial or financial relationships that could be construed as a potential conflict of interest.

References

1. Maliyekkal, S.M.; Lisha, K.P.; Pradeep, T. A Novel Cellulose–Manganese Oxide Hybrid Material by in Situ Soft Chemical Synthesis and Its Application for the Removal of Pb(II) from Water. *J. Hazard. Mater.* **2010**, *181*, 986–995. [CrossRef]
2. Li, P. Study on the High-Efficiency Separation of Fe and Mn from Low-Grade Pyrolusite and the Preparation of $LiMn_2O_4$ Materials for Lithium-Ion Batteries. *Sep. Purif. Technol.* **2022**, *278*, 119611. [CrossRef]
3. Shi, X.; Lv, Y.; Zhang, Y.; Liu, X.; Dong, Z.; Zhang, X. Role of Mn in Improving the Corrosion Resistance and Cytocompatibility of Antibacterial Mg-Ag-Mn Alloy. *J. Alloys Compd.* **2024**, *1008*, 176590. [CrossRef]
4. Wang, M.; Meng, Y.; Xu, Y.; Chen, N.; Chuai, M.; Yuan, Y.; Sun, J.; Liu, Z.; Zheng, X.; Zhang, Z.; et al. Aqueous All-Manganese Batteries. *Energy Environ. Sci.* **2023**, *16*, 5284–5293. [CrossRef]
5. Sun, B.; Kwiatkowski, D.S.A.; Wu, Y.; Ma, Y.; Chen, H.; Scott, C.; Ponge, D.; Raabe, D. Physical Metallurgy of Medium-Mn Advanced High-Strength Steels. *Int. Mater. Rev.* **2023**, *68*, 786–824. [CrossRef]
6. Edelstein, D.; Heidenreich, J.; Goldblatt, R.; Cote, W.; Uzoh, C.; Lustig, N.; Roper, P.; McDevitt, T.; Motsiff, W.; Simon, A.; et al. Full Copper Wiring in a Sub-0.25 Mm CMOS ULSI Technology. In *Proceedings of the International Electron Devices Meeting. IEDM Technical Digest*; IEEE: New York, NY, USA, 1997; pp. 773–776.
7. Kowalik, P.; Kopyto, D.; Ciszewski, M.; Drzazga, M.; Leszczyńska-Sejda, K. Purification of Industrial Copper Electrolyte from Bismuth Impurity. *Minerals* **2022**, *12*, 36. [CrossRef]
8. Cao, X. Electrorefining of High Purity Manganese. *Hydrometallurgy* **2017**, *171*, 412–421. [CrossRef]
9. Shi, G.; Wang, J.; Zhang, S.; Cheng, J.; Shao, X.; Xu, Z.; Chen, X.; Xin, B. Green Regeneration and High-Value Utilization Technology of the Electrolyte from Spent Lithium-Ion Batteries. *Sep. Purif. Technol.* **2024**, *335*, 126144. [CrossRef]
10. Han, W.; Zhang, Y.; Liu, R.; Sun, Y.; Li, M. Purification of Spent Electrolyte by Sequential Precipitation Method and Its On-Line Monitoring. *Ionics* **2021**, *27*, 4829–4838. [CrossRef]
11. Zhang, W.; Cheng, C.Y. Manganese Metallurgy Review. Part I: Leaching of Ores/Secondary Materials and Recovery of Electrolytic/Chemical Manganese Dioxide. *Hydrometallurgy* **2007**, *89*, 137–159. [CrossRef]
12. Lu, J.; Dreisinger, D.; Glück, T. Manganese Electrodeposition—A Literature Review. *Hydrometallurgy* **2014**, *141*, 105–116. [CrossRef]
13. Krstić, V.; Pešovski, B. Reviews the Research on Some Dimensionally Stable Anodes (DSA) Based on Titanium. *Hydrometallurgy* **2019**, *185*, 71–75. [CrossRef]
14. Wu, T.; Ma, B.; An, Y.; Chen, Y.; Wang, C. Improvement of Manganese Electrolytic Process and Secondary Resources Recovery of Manganese: A Review. *Process Saf. Environ. Prot.* **2024**, *186*, 895–909. [CrossRef]
15. Ayalew, Z.M.; Zhang, X.; Guo, X.; Ullah, S.; Leng, S.; Luo, X.; Ma, N. Removal of Cu, Ni and Zn Directly from Acidic Electroplating Wastewater by Oligo-Ethyleneamine Dithiocarbamate (OEDTC). *Sep. Purif. Technol.* **2020**, *248*, 117114. [CrossRef]
16. Leng, S.; Guo, X.; Li, B.; Wu, X.; Kong, Z. Sequestration of Various Heavy Metals from Wastewater Using a Newly Developed Oligo-Dithiocarbamate: A Comprehensive Survey under Acidic and Complexation Conditions. *J. Environ. Manag.* **2025**, *383*, 125525. [CrossRef]
17. Wang, W.; Huang, C. Treatment of Wastewater Containing Heavy Metal Ions by Chelate Precipitation. *China Water Wastewater* **2002**, *18*, 49–50.
18. Lin, H.; Zhang, Y.; He, Y.; Dong, Y. Research Progress of Heavy Metal Collectors in Wastewater Treatment. *Technol. Water Treat.* **2020**, *46*, 6. [CrossRef]
19. Ni, T. Experimental Study on Treatment of Mine Wastewater by DTCR-2. Master's Thesis, Nanchang University, Nanchang, China, 2014.
20. Samrane, K.; Bouhaouss, A. Highly Selective Complexation of Cadmium from Wet Phosphoric Acid by Organic Coordination Ligands. *Miner. Eng.* **2022**, *189*, 107858. [CrossRef]
21. Zhang, X.; Zeng, L.; Wang, Y.; Tian, J.; Wang, J.; Sun, W.; Han, H.; Yang, Y. Selective Separation of Metals from Wastewater Using Sulfide Precipitation: A Critical Review in Agents, Operational Factors and Particle Aggregation. *J. Environ. Manag.* **2023**, *344*, 118462. [CrossRef]
22. Chen, C.; Zhang, L.; Xiang, H.; Zhang, Z.; Wang, J.; Wang, J. Research Progress on Application of Sodium Dimethyldithiocarbamate in Heavy Metal Removal. *Environ. Prot. Chem. Ind.* **2025**, *45*, 481–487. [CrossRef]
23. Rayner-Canham, G.; Overton, T. *Descriptive Inorganic Chemistry*, 6th ed.; W.H. Freeman and Company: New York, NY, USA, 2014.

24. Yang, Y.; Liu, R.; You, Y.; Nong, R.; Li, C.; Wei, H.; Luo, J.; Luo, H.; Yang, H.; Chen, S.; et al. Preparation of High-Purity Manganese Sulfate Using Electrolytic Manganese Anode Slime: Leaching Mechanism and Impurity Removal Rule. *Ind. Eng. Chem. Res.* **2025**, *64*, 13410–13420. [CrossRef]
25. Domingo, L. Molecular Electron Density Theory: A Modern View of Reactivity in Organic Chemistry. *Molecules* **2016**, *21*, 1319. [CrossRef] [PubMed]
26. He, J.; Zhang, C.; Song, S.; Sun, W.; Hu, Y.; Lei, S.; Yang, Y. Computational and Experimental Investigation of Dimethyldithiocarbamate for Effective Recovery of Cobalt and Nickel from the Leach Liquor of High Manganese Slag. *Sep. Purif. Technol.* **2019**, *223*, 55–62. [CrossRef]
27. Liu, J.; Wang, Y.; Luo, D.; Zeng, Y.; Wen, S.; Chen, L. DFT Study of SDD and BX Adsorption on Sphalerite (1 1 0) Surface in the Absence and Presence of Water Molecules. *Appl. Surf. Sci.* **2018**, *450*, 502–508. [CrossRef]
28. Zhang, X.; Xiong, W.; Lu, L.; Qian, Z.; Zhu, Y.; Mkhonto, P.P.; Zheng, Y.; Han, L.; Ngoepe, P.E. A Novel Synthetic Polymer Depressant for the Flotation Separation of Chalcopyrite and Galena and Insights into Its Interfacial Adsorption Mechanism. *Sep. Purif. Technol.* **2021**, *279*, 119658. [CrossRef]
29. Fu, K.; Chen, M. Investigation on Decontamination Kinetics of Metallic Radionuclides in Irradiated Graphite by Chlorination Roasting. *Sep. Purif. Technol.* **2024**, *330*, 125430. [CrossRef]
30. Clancy, M.; Bettles, C.J.; Stuart, A.; Birbilis, N. The Influence of Alloying Elements on the Electrochemistry of Lead Anodes for Electrowinning of Metals: A Review. *Hydrometallurgy* **2013**, *131–132*, 144–157. [CrossRef]
31. Zheng, F.; Li, Y.; Wang, D.; Li, J.; Zhu, H. The Effects of Zn^{2+} and Polyacrylamide (PAM) on the Electrodeposition of Manganese from Non-Selenium Sulfate Solutions. *Int. J. Electrochem. Sci.* **2018**, *13*, 1879–1892. [CrossRef]
32. Halls, D.J. The Properties of Dithiocarbamates a Review. *Mikrochim. Acta* **1969**, *57*, 62–77. [CrossRef]
33. Jones, M.M.; Burka, L.T.; Hunter, M.E.; Basinger, M.; Campo, G.; Weaver, A.D. Dithiocarbamate Chelating Agents for Toxic Heavy Metals. *J. Inorg. Nucl. Chem.* **1980**, *42*, 775–778. [CrossRef]
34. Kanchi, S.; Singh, P.; Bisetty, K. Dithiocarbamates as Hazardous Remediation Agent: A Critical Review on Progress in Environmental Chemistry for Inorganic Species Studies of 20th Century. *Arab. J. Chem.* **2014**, *7*, 11–25. [CrossRef]

Disclaimer/Publisher's Note: The statements, opinions and data contained in all publications are solely those of the individual author(s) and contributor(s) and not of MDPI and/or the editor(s). MDPI and/or the editor(s) disclaim responsibility for any injury to people or property resulting from any ideas, methods, instructions or products referred to in the content.